fibers

Article

Modeling and Analysis of the Transverse Surface Roughness in Hollow-Core Fibers

Federico Melli [1], Kostiantyn Vasko [2,3], Lorenzo Rosa [1], Fetah Benabid [2,3] and Luca Vincetti [1,*]

[1] Department of Engineering "Enzo Ferrari", University of Modena and Reggio Emilia, 41125 Modena, Italy; lorenzo.rosa@unimore.it (L.R.)
[2] GPPMM Group, XLIM Resaerch Institute, CNRS UMR 7252, 123 Avenue Albert Thomas, 87060 Limoges, France; kostiantynvasko@glophotonics.fr (K.V.); f.benabid@xlim.fr (F.B.)
[3] GLOphotonics, 123 Avenue Albert Thomas, 87060 Limoges, France
* Correspondence: luca.vincetti@unimore.it

Abstract: The corrugation of the interfaces of the cross-section of hollow core fibers based on the inhibited coupling waveguiding mechanism is modeled and the impact on propagation loss analyzed. The proposed model is based on a combined use of coupled-mode theory and Azimuthal Fourier Decomposition. It shows that such transverse roughness causes coupling between the core modes and the dielectric modes of the cladding and consequently an increase of the fiber loss. The model is validated by comparing theoretical and numerical results obtained by applying both deterministic and stochastic corrugations to tubular lattice and nested fibers. Scaling laws and impact of the fibers' parameters are discussed. The model shows that the loss increase is not directly correlated to the root mean square of the stochastic roughness but only to the value of the power spectral density in specific spatial frequency ranges. In particular, the spectral components characterized by a periodicity lower than 10^{-1} of the tube circumference must have a power spectral density value lower than 0.2 nm^2 to ensure a negligible effect of the transverse roughness on fibers with losses lower than 0.1 dB/Km.

Keywords: optical fibers; hollow-core fibers; inhibited coupling fibers; fiber properties; loss; roughness

check for updates

Academic Editors: Paulo Caldas and Mario F. S. Ferreira

Received: 15 October 2024
Revised: 10 March 2025
Accepted: 21 March 2025
Published: 27 March 2025

Citation: Melli, F.; Vasko, K.; Rosa, L.; Benabid, F.; Vincetti, L. Modeling and Analysis of the Transverse Surface Roughness in Hollow-Core Fibers. *Fibers* **2025**, *13*, 36. https://doi.org/10.3390/fib13040036

1. Introduction

In the last fifteen years, hollow-core photonic crystal fibers based on the inhibited coupling guidance mechanism (IC-HCPCF) have experienced an impressive loss reduction, recently overtaking the Rayleigh scattering limit on a wide range of wavelengths, spanning from UV and visible [1] to near-infrared [2–4]. At first, researchers' efforts were focused on confinement loss (CL) reduction. CL is the only loss mechanism in ideal IC-HCPCFs. The introduction of the negative curvature core-cladding interface [5], together with the proposal first [6] and fabrication soon after [7] of tube lattice fibers (TLFs), followed by the conceptualization and fabrication of nested [8], node-less [9] and conjoint tubes [10] fibers, pushed CL down by several orders of magnitude. The other main family of hollow-core fibers, called photonic bandgap fibers (PBGFs), differentiates from ICFs since the cladding does not exhibit a continuum of modal solutions, but instead exhibits a photonic bandgap (PBG) wherein cladding modes are completely absent [11–13]. Thus, one of the two matching conditions with the core mode, that of phase matching between the core mode and a cladding mode having the same effective index, cannot be fulfilled, which nullifies the overlap integral between the two. In the early stages of HCF research, PBGFs enjoyed lower confinement loss than ICFs; however, over time the lower dielectric power fraction and wider transmission bandwidth of ICFs proved more advantageous for hollow-core fiber low-loss applications.

Gradually, the research effort moved toward other loss mechanisms caused by imperfect manufacturing processes and thus not occurring in ideal fibers. Currently, the two main mechanisms identified by the research community are microbending loss (MBL) and surface scattering loss (SSL). MBL is a stochastic phenomenon consisting in microscopic and random deflections of the fiber axis from the ideal straight longitudinal direction. The axis deflection introduces a coupling of the fundamental core mode (FCM) with other modes, causing a power drainage which increases the propagation loss [14,15]. SSL originates from the fact that the interfaces of the microstructured cladding are not completely flat, as assumed in ideal fibers, but exhibit a random corrugation. This roughness is generated by frozen-in thermal surface capillary waves (SCWs) caused by the interplay between thermal noise and glass interface surface tension as the fiber is drawn [16–18]. Due to its thermodynamic cause, surface roughness cannot be completely eliminated. However, recently a new drawing technique based on counter-directional gas and dielectric flows during fiber drawing has been proposed and implemented, showing a significant reduction in surface roughness [1]. So far, all the modeling based both on rigorous [15,19] and heuristic approaches [9,14] focused on the effect of surface roughness along the propagation direction, usually identified with the z-axis (z-roughness). On the surfaces, there is also a transverse roughness (t-roughness), related to the stochastic corrugation on the transverse plane and affecting the fiber cross-section. Additionally, the experimental data collected on surface roughness are too limited to provide a comprehensive overview of the surface topology. Indeed, the roughness measurement attempts were limited to 10^{-3} μm [20–23] in the low-frequency range and to 100 μm in the higher spatial frequency range, making a complete model of the roughness challenging. Furthermore, unlike z-roughness, t-roughness has been until now scarcely investigated [24].

In this context, this work presents a theoretical model on t-roughness's impact on TLF-like IC-HCPCF loss. The model demonstrates that transverse roughness perturbs the fiber structure in a way that induces coupling between the fundamental core mode and cladding dielectric modes, ultimately increasing confinement loss (CL). On the other hand, the coupling induced by the transverse roughness is not strong enough to perturb the effective refractive index of the fundamental mode and thus the dispersion. In inhibited coupling fibers, light is effectively confined because the cladding is populated by high-azimuthal-index DMs, which naturally inhibit coupling with the core mode [25]. However, transverse roughness modifies the cladding boundaries. By decomposing the roughness perturbation into its Fourier components, the model establishes that only roughness components with specific spatial frequencies contribute to mode coupling. In particular, only the high-frequency components of the roughness PSD can effectively couple with the high azimuthal index dielectric modes in the cladding. This occurs because these roughness components satisfy the phase-matching condition necessary for efficient energy transfer from the core mode to lossy dielectric cladding modes. More precisely, the results show that roughness components with spatial periodicities larger than approximately 10^{-1} of the cladding tube circumference do not significantly affect loss, as their spectral energy is too low to interact with the relevant cladding modes. Conversely, higher-frequency roughness components strongly enhance the power transfer from the core mode to the DMs, leading to increased propagation loss. This explains why CL is not simply a function of the roughness amplitude (RMS value), but rather a consequence of the roughness spectral distribution. Finally, the model is validated through numerical simulations, quantifying the impact of t-roughness on loss for both tube lattice fibers (TLFs) and nested fibers. These findings emphasize the crucial need to control high-frequency roughness components in order to maintain ultra-low-loss performance in inhibited coupling fibers. Finally, the model is validated through numerical simulations, and the impact of t-roughness on loss is quantified for both Tube Lattice Fibers (TLFs) and nested fibers, demonstrating the applicability of the findings across different fiber architectures. All the simulations were performed using Comsol Multiphysics modal solver with the simulation domain surrounded by PML.

2. Modeling

For the sake of analysis, let us consider a tube lattice fiber (TLF). The basic cross-section and the geometrical parameters are shown in Figure 1. This kind of IC-HCPCF consists in an arrangement of N_t elements separating the hollow core from the homogeneous external jacket, with the goal to decouple as much as possible the light confined in the core from the continuum of radiating waves in the jacket.

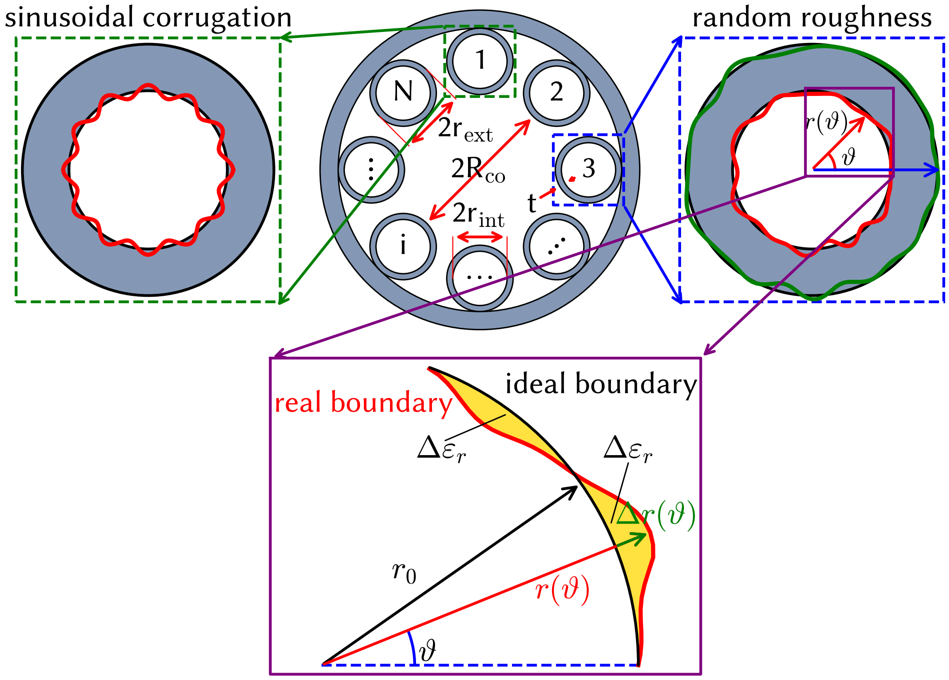

Figure 1. Top: Fiber cross-section with geometrical parameters. Gray regions refer to dielectric with refractive index n_d, white ones to a material with $n_g = 1$. The right inset shows an example of a tube whose boundaries are affected by transverse roughness, together with the employed local polar frame of reference. The left inset shows a tube with only the inner boundary affected by a perfect sinusoidal corrugation. **Bottom**: detail of the surface with random roughness and representation in terms of the local polar frame of reference and the displacement $\Delta r(\theta)$.

Let us assume that the tube interfaces are affected by a deformation due to roughness on the transverse plane, as shown in the right inset of Figure 1. In the context of single tube approximation [26], and by assuming the roughness in each tube is uncorrelated with that in the other ones, each tube can be analyzed separately. By introducing a local polar frame of reference (r, θ) centered at the center of the tube and shown in Figure 1, the deformation is described by a displacement $\Delta r(\theta)$ of the real surface outlined by the function $r(\theta)$ with respect to the perfectly circular ideal one with radius $r_0 = r_{int},\ r_{ext}$ for the inner and outer surface, respectively. In the context of coupled-mode theory (CMT) [27,28], this can be modeled in terms of a dielectric permittivity perturbation:

$$\Delta\epsilon = \epsilon_r^{real} - \epsilon_r^{ideal} \tag{1}$$

where ϵ_r^{real} is the function describing the permittivity of the real fiber and ϵ_r^{ideal} is that of the ideal one. The perturbation can cause coupling among the fiber modes. Even though the approach is completely general, here, for the sake of simplicity, we focus on the effects of FCM coupling to DMs [26].

DMs feature two different polarizations, called EH and HE, and are described by two indices μ and ν. EH and HE polarizations have the dominant electric field component aligned along the radial and azimuthal direction, respectively. The azimuthal index μ corresponds to the number of periods that the dominant electric field component shows along the azimuthal direction, and the radial index ν is the total number of maxima and minima of the dominant electric field component along the radial direction.

2.1. Coupling Coefficient Calculation

Let us consider the coupling between the FCM and the DM having indices μ and ν. The DM polarization can be either EH or HE. The coupling coefficient is

$$k = \frac{\pi}{2\eta_0}\frac{1}{\lambda}\iint_{S_d} \Delta\epsilon_r \overline{E}_{FCM} \cdot \overline{E}^*_{DM} dS, \tag{2}$$

where η_0 is the free space impedance, λ is the wavelength, $\overline{E}_{FCM}$ and $\overline{E}_{DM}$ are the power-normalized electric field transverse components of the FCM and CLM of the ideal fiber, respectively, and S_d is the region of the fiber cross-section where $\Delta\epsilon_r \neq 0$. On each of the two interfaces, the perturbation can be written as

$$\Delta\epsilon_r = -q\begin{cases}(1-n_d^2);\ \text{if } r_0 < r(\theta) < r_0+\Delta r(\theta) \text{ and } \Delta r \geq 0\\[2ex] (n_d^2-1);\ \text{if } r_0+\Delta r(\theta) < r(\theta) < r_0 \text{ and } \Delta r < 0\end{cases}$$

with

$$q = \begin{cases}-1 \text{ if } r_0 = r_{ext}\\ \ \ 1 \text{ if } r_0 = r_{int}\end{cases}$$

We assume $\Delta r << t, \lambda$, and r_0; in that case, the core and cladding mode field distributions can be assumed to be almost constant between r_0 and $r_0 + \Delta r$: $\overline{E}_{FCM}(r,\theta) \simeq \overline{E}_{FCM}(r_0,\theta)$, $\overline{E}_{DM}(r,\theta) \simeq \overline{E}_{DM}(r_0,\theta)$, and Equation (2) can be approximated as

$$k \simeq \frac{q\pi}{2\eta_0}\frac{n_d^2-1}{r_0\lambda}\int_0^{2\pi} \overline{E}_{FCM}(r_0,\theta)\cdot\overline{E}^*_{DM}(r_0,\theta)\Delta r(\theta)d\theta. \tag{3}$$

In order to analyze how the value of the integral in Equation (3), and thus the coupling strength, depends on the FCM and DM field distributions, the azimuthal Fourier decomposition (AFD) [29] can be applied to the radial and azimuthal components E^r_{FCM} and E^θ_{FCM} of the FCM and to the perturbation $\Delta r(\theta)$:

$$E^s_{FCM}(r_0,\theta) = \sum_{m=-\infty}^{+\infty} R^s_m e^{-jm\theta}, \tag{4}$$

$$\Delta r(\theta) = \sum_{m=-\infty}^{+\infty} C_m e^{-jm\theta}, \tag{5}$$

with $s = r, \theta$. The sets $\{R^s_m\}$ and $\{C_m\}$ contain the azimuthal Fourier spectra (AFS) of the FCM electric field components and of the perturbation calculated on the circle of radius r_0. They represent the amplitude of the spatial harmonics at spatial frequency $\tilde{f} = m/(2\pi r_0)$ and depend on the field profile and on the kind of roughness on the interface, respectively.

Figure 2 shows an example of the FCM AFS. It refers to the y-polarized FCM and is calculated on the boundaries of tube 1 in Figure 1. More details about AFS and AFD can be found in [29]. Even though the spectra of the two components have different shapes, both of them show a "low pass" kind of spectrum, meaning that the AFS coefficients rapidly decrease for increasing m. Values of $m > 5 \div 6$ guarantee that the corresponding R^s_m will have values more than one order of magnitude lower than the maximum. The C_m coefficients depend on the specific perturbation affecting the considered boundary, which will be analyzed in the following sections.

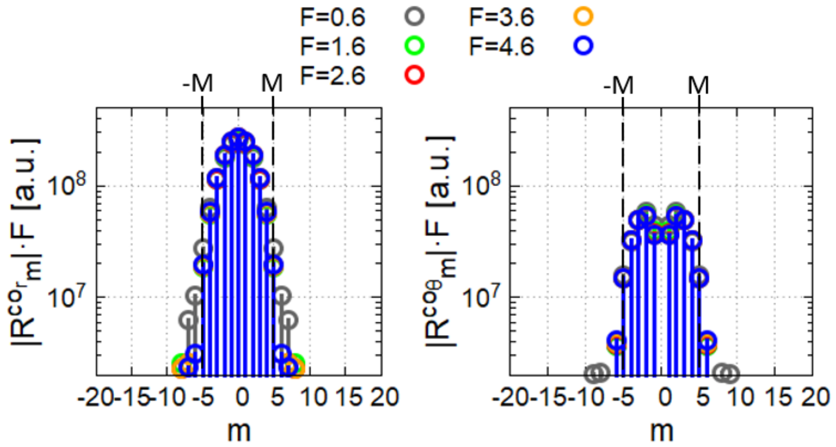

Figure 2. AFS of the radial (**left**) and azimuthal (**right**) components of the FCM, calculated at the inner and outer boundaries of tube 1 with no surface roughness for different normalized frequencies.

The DM electric field components for a single isolated tube are analytically known [30] and can be written in the following form:

$$E^s_{DM}(r_0, \theta) = A^s e^{j\mu\theta}. \tag{6}$$

By substituting Equations (4)–(6) into Equation (3), and recalling that

$$\int_0^{2\pi} e^{-jn\theta} d\theta = \begin{cases} 0 & \text{if } n \neq 0 \\ 2\pi & \text{if } n = 0 \end{cases}$$

it yields

$$k = \frac{q\pi r_0}{\eta_0 \lambda}(n_d^2 - 1)\left(g^\theta + g^r\right), \tag{7}$$

with

$$g^s = A^s \sum_m R^s_{\mu-m} C_m. \tag{8}$$

2.2. Loss Calculation

Mode coupling, quantified by coefficient k, causes a variation in the FCM attenuation constant. It can be shown that, in that case, the attenuation constant can be written as [25]

$$\alpha'_{FCM} = \alpha_m - \frac{1}{2}\Im\left(\sqrt{(\Delta\beta - j\Delta\alpha)^2 + (2k)^2}\right). \tag{9}$$

At the phase matching condition ($\Delta\beta = 0$), under the assumption that $2|k| << \Delta\alpha$ and $\alpha_{FCM_0} << \alpha_{DM_0}$, Equation (9) is simplified as

$$\alpha'_{FCM} = \alpha_{FCM_0} + \delta\alpha, \tag{10}$$

where α_{FCM_0} and α_{DM_0} are the FCM and DM attenuation constants at the phase matching condition in the ideal fiber, respectively, and

$$\delta\alpha = \left(\frac{|k|}{\alpha_{DM_0}}\right)^2 \tag{11}$$

is the additional loss due to roughness. By substituting Equation (7) into Equation (11), the expression of the additional loss at the phase matching condition, due to the FCM coupling with a DM as caused by t-roughness, is obtained:

$$\delta\alpha_i = \left[\frac{D}{\lambda}\left(g_i^{\theta} + g_i^{r}\right)\right]^2, \tag{12}$$

where $D = \pi(n_d^2 - 1)r_0/(\eta_0\alpha_{DM_0})$. The subscript "$i$" indicates that the quantity refers specifically to the loss increase due to the coupling between the FCM and the i-th DM having polarization either EH or HE and indices μ and ν. When the phase-matching condition is not fulfilled, according to Equation (9), the additional loss is reduced and the expression becomes

$$\delta\alpha^i(F) = \left[\frac{D}{\lambda}\left(g_i^{\theta} + g_i^{r}\right)L(F - F_{c_i})\right]^2, \tag{13}$$

where $L(F)$ is a normalized function ($L(0) = 1$) which rapidly decreases for increasing F [25] and can be locally approximated by a Lorentzian function [26]. F_{c_i} is the cutoff frequency of the i-th DM.

The total additional loss α_{tr} due to t-roughness is the sum of all the contributions:

$$\alpha_{tr} = \frac{1}{\lambda^2}\sum_i\left[D_i\left(g_i^{\theta} + g_i^{r}\right)L(F - F_{c_i})\right]^2. \tag{14}$$

The sum is intended to include all DMs and fiber interfaces.

2.3. Scaling Laws

The dependence of α_{tr} on the fiber's parameters is given by Equation (14). According to Equation (8), the contributions of the square of the g parameter scale as R_m^2, which depends on the square of the electric field on the interfaces [29]. The trend of the latter can be effectively estimated by the integral of the square of the electric field on the interfaces F_{cc} [30]:

$$F_{cc} = \sqrt{\frac{\epsilon_0}{\mu_0}}\,\frac{\oint_\Gamma |\overline{E}|^2 d\Gamma}{\iint_{S_\infty} p_z}. \tag{15}$$

According to an empirical formula, the minimum of F_{cc} in each TB scales as λ^2/R_{co}^3 [31]. Combining all the dependencies gives

$$\alpha_{tr} \propto \frac{1}{R_{co}^3}. \tag{16}$$

This shows that α_{tr} does not depend on wavelength, while it rapidly decreases for increasing core size. Since the minimum of CL in each TB in ideal TLFs scales as $\lambda^{4.5}/R_{co}^4$ [31], the effects of t-roughness, compared to those of CL, tend to be more and more significant as wavelength is reduced and core radius is increased.

3. Sinusoidal Corrugation

To gain insight into the coupling mechanism caused by the transverse roughness, it is better to start with a simplified but very useful case. It is shown in the left inset of Figure 1, and it consists of a perfectly sinusoidal perturbation applied only on the inner surface of tube 1:

$$\Delta r(\theta) = A_P cos(P\theta), \tag{17}$$

where P is the number of periods along the tube boundary, resulting in a spatial frequency $\tilde{f}_P = P/(2\pi r_0)$. Notice that any such kind of perturbation must be periodic within the circumference $2\pi r_0$ and it can always be modeled as a linear superposition of sinusoidal corrugations.

The corresponding AFS has just two nonzero coefficients, for $m = \pm P$: $C_P = C_{-P} = A_P/2$. Substituting them into Equation (8) and then in (12) yields the amplitude of the loss peak, centered at $F = F_{c_{\mu,\nu}}$:

$$\delta\alpha_{\mu,\nu} = D^2 \left(\frac{A_P}{2}\right)^2 \left(A^{\theta}_{\mu,\nu} R^{\theta}_{\mu-P} + A^{r}_{\mu,\nu} R^{r}_{\mu-P}\right)^2. \tag{18}$$

Equation (18) can be further simplified by observing that EH polarized DMs have $A_r >> A_\theta$, and the opposite is true for the HE ones, so that

$$\delta\alpha^{EH}_{\mu,\nu} \simeq D^2 \left(\frac{A_P}{2}\right)^2 \left(A^{r}_{\mu,\nu} R^{r}_{\mu-P}\right)^2; \tag{19}$$

$$\delta\alpha^{HE}_{\mu,\nu} \simeq D^2 \left(\frac{A_P}{2}\right)^2 \left(A^{\theta}_{\mu,\nu} R^{\theta}_{\mu-P}\right)^2. \tag{20}$$

From the previous equations, it emerges that, despite the perturbation being purely sinusoidal, the additional loss function $\delta\alpha$ is composed of a sequence of peaks having amplitude given by Equations (19) and (20), centered at the cutoff frequencies of the involved DMs. The peak amplitudes are shaped by the FCM AFS of the fiber perturbed with this sinusoidal surface roughness. The equations show that the FCM AFS is "spectrally translated" at the cutoff frequency of the DM with $\mu = P$. The number of DMs giving a significant contribution is however limited by the low-pass "filtering" given by the FCM AFS. Roughly, only the DMs with $P - M < \mu < P + M$ for $M = 5 \div 6$ give a significant contribution to the additional loss [29,32].

To clarify this concept and validate the model, let us consider Figure 3. It refers to a fiber, hereinafter named Fiber #1, with parameters $R_{co} = 24.5$ µm, $r_{ext} = 10$ µm, $t = 0.5$ µm, $n_d = 1.45$, and $n_g = 1.0$. Panel (c) compares the CL spectra of an ideal and a sinusoidally perturbed fiber with $P = 50$. The two spectra coincide everywhere except for some narrow peaks. The peaks here highlighted correspond to the effects of the coupling of the FCM with specific EH DMs, given by Equation (19). The loss peak shapes perfectly match the shape of the AFS of the radial component of the FCM but shifted by $m = P = 50$ from the FCM AFS of roughness-free case (see the left plot in Figure 2, and the blue and black spectra in panel (a)). Panel (b) shows the $\mu - F_c$ curves of the DMs, highlighting the correspondence between the azimuthal index μ of the DMs and their cutoff frequencies $F_{c_{\mu,\nu}}$ [25]. As we deal with EH DMs only, the curves with empty circles must be considered. The correspondence between the coefficients in panel (a) and the spectral collocations of the peaks in panel (c) is very good. The different peaks in the different TBs are due to the coupling of the FCM with DMs having same μ but different ν. Since the slopes of the $\mu - F_c$ curves increase for increasing ν, the peaks change position in the different TBs and shift toward lower frequencies as the order of the TB, and thus the value of ν, is increased. Panel (d) shows the real and imaginary part of $\overline{E}_{FCM}$ at $F = 1.745$, corresponding to the peak maximum. The imaginary part shows the hybridization with DM $EH_{50,2}$; that is, the one having $\mu = P$, due to the coupling, coherently with the theoretical model. Finally, in panel (c), losses obtained from Equation (19) are also reported. The agreement with the numerical results is excellent.

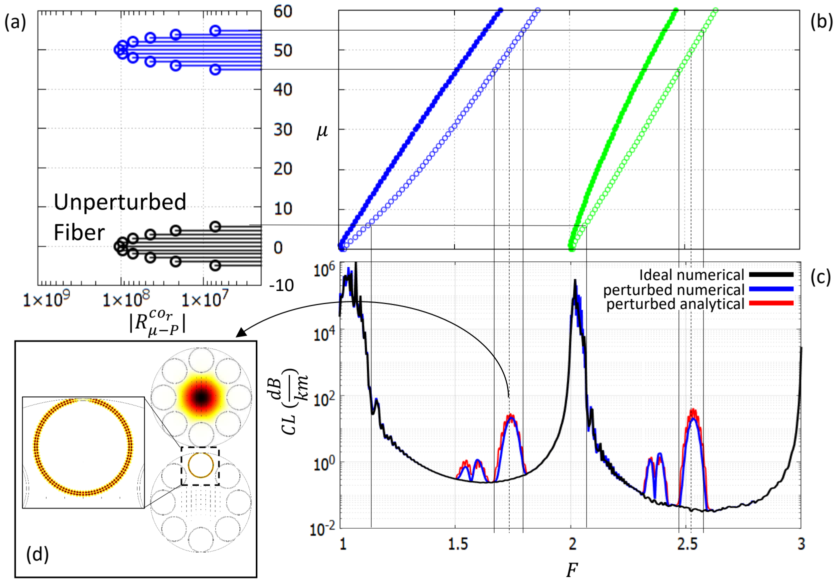

Figure 3. Fiber #1 having a sinusoidal perturbation with amplitude $A_P = 0.005t$ and number of periods $P = 50$. (**a**): Azimuthal spectrum of the y-polarized FM azimuthal component at F = 1.745 and F = 2.6 (blue spectrum) and 1.1 and 2.1 (black spectrum). (**b**): Azimuthal index μ versus cutoff frequency F_c of HE (filled circles) and EH (empty circles) DMs having $\nu = 2$ (blue) and $\nu = 3$ (green). (**c**): CL spectra of the ideal (black) and perturbed (red) fiber. (**d**): Real and imaginary part of the FM electric field of the perturbed fiber calculated at frequency $F = 1.745$, corresponding to the cutoff frequency of the $EH_{50,2}$ mode. The inset shows a detail of the perturbed tube.

Figure 4 shows the same fiber, in the same condition, but focusing on the coupling with HE DMs. According to Equation (20), now the peaks are shaped by the AFS of the FM azimuthal component (see the right plot in Figure 2), spectrally shifted by $m = P = 50$ and shown in panel (a). In this case, the HE $\mu - F_c$ curves (filled circles) must be considered, and since they have higher slope than the EH ones, the peaks are at lower frequencies. Also in this case, the shape of the peaks follows the AFS one and the losses predicted by Equation (20) are again in good agreement with the numerical results.

The amplitudes are lower since the AFS coefficients of the azimuthal FCM component are smaller when compared to the radial ones for the chosen tube and FCM polarization [29]. In R^{θ}_{m}, the central coefficient ($m = 0$) is zero, and the maximum of $\delta\alpha$ occurs for $m = 50$, corresponding to the coupling with DMs $HE_{50,\nu}$. Figure 4 shows the FCM filed at $F = 1.6$ that is the F_c of $HE_{50,2}$. Once again, the imaginary part shows the hybridization of the FCM with the DM expected by the theoretical model. Similar results are obtained for the x-polarized FCM, just by interchanging the roles of the azimuthal and radial components. It is important to highlight the role played by the $\mu - F_c$ curves. They represent the relationship between the DM indices μ, ν and the DM cutoff frequencies $F_{c_{\mu,\nu}}$, and, in the context of the proposed model, the manner in which the AFS defined in the AFD domain (m index) are mapped to the normalized frequency F domain, resulting in the additional loss spectra.

To complete the analysis and to clarify this crucial aspect, a second fiber (Fiber #2) with the same geometrical parameters as Fiber #1, but having $n_d = 2.45$, is analyzed in Figure 5. The change in the dielectric refractive index n_d significantly modifies the $\mu - F_c$ curves of the EH DMs. The same effect, involving in this case both EH and HE DMs, occurs by changing the tube aspect ratio $\rho = r_{int}/r_{ext}$, but with weaker impact and is not discussed here. The different $\mu - F_c$ curves change the correspondence between azimuthal index and cutoff frequencies, so in order to show peaks in the same TBs, a corrugation with a lower number of periods, $P = 32$, was considered. The agreement both in terms of shape and spectral collocation is confirmed. Notice that the peaks due to the coupling with HE modes are not visible in the perturbed fiber spectrum of Figure 5c. In fact, due to the different shape of the HE $\mu - F_c$ curves, such peaks fall in the high loss regions and so the effects of $\delta\alpha$ are negligible.

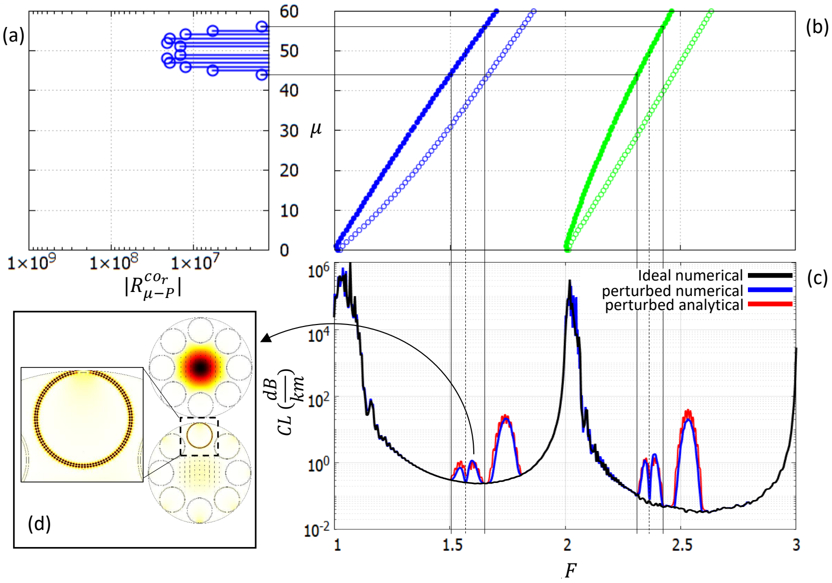

Figure 4. Fiber #1 having a sinusoidal perturbation with amplitude $A_P = 0.005t$ and number of periods $P = 50$. (**a**): Azimuthal spectrum of the y-polarized FM azimuthal component. (**b**): Azimuthal index μ versus cutoff frequency F_c of HE (filled circles) and EH (empty circles) DMs having $\nu = 2$ (blue) and $\nu = 3$ (green). (**c**): CL spectra of the ideal (black) and perturbed (red) fiber. (**d**): Real and imaginary part of the FM electric field of the perturbed fiber calculated at frequency $F = 1.6$, corresponding to the cutoff frequency of the $HE_{50,2}$ mode. The inset shows a detail of the perturbed tube.

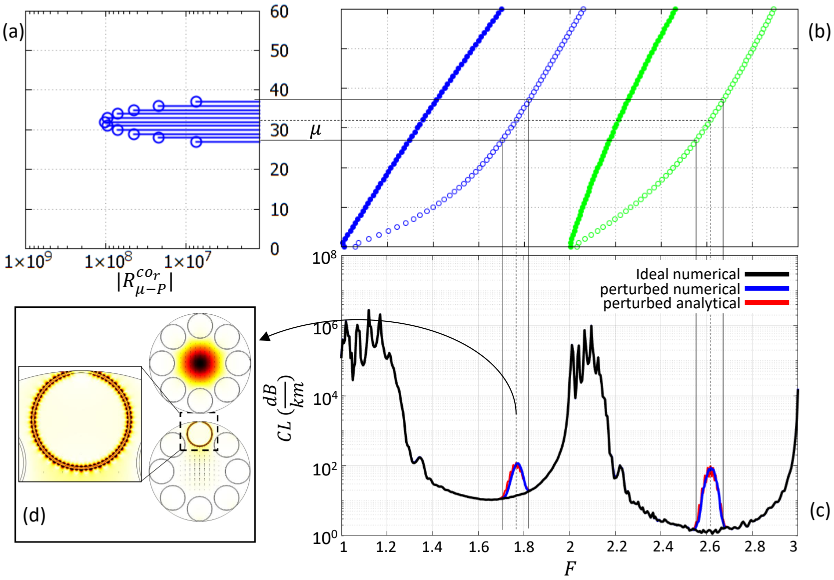

Figure 5. Fiber #2 having a sinusoidal perturbation with amplitude $A_P = 0.05t$ and number of periods $P = 32$. (**a**): Azimuthal spectrum of the y-polarized FM azimuthal component. (**b**): Azimuthal index μ versus cutoff frequency F_c of HE (filled circles) and EH (empty circles) DMs having $\nu = 2$ (blue) and $\nu = 3$ (green). (**c**): CL spectra of the ideal (black) and perturbed (red) fiber. (**d**): Real and imaginary part of the FM electric field of the perturbed fiber calculated at frequency $F = 1.765$, corresponding to the cutoff frequency of the $EH_{32,2}$ mode. The inset shows a detail of the perturbed tube.

On the basis of those observations, an important result must be highlighted. Recalling that the effects of the corrugation are noticeable only when the peaks fall in the TBs, and that the lobes are quite narrow ($M \sim 5 \div 6$) and are spectrally located at the cutoff frequencies $F_{c_{P,\nu}}$ of the DMs with $\mu = P$, it follows that only the corrugations with spatial period P such that $F_{c_{P,\nu}}$ falls in TBs cause noticeable additional loss. The concept is illustrated in Figure 6. Just to give a reference, let us define the extension of each TB as the frequency range where losses are lower than ten times the minimum loss for that TB. Light red, light blue and light green regions highlight those ranges and, through the $\mu - F_c$ curves, the P values giving $F_{c_{P,\nu}}$ within the defined TBs. Even though the values depend on TB spectral extension and $\mu - F_c$ curve slope, speaking in the broadest sense, non-negligible contributions occur for $P \geq P_{min}$ with $P_{min} \sim 10$. In terms of spatial frequency $\tilde{f}$, it means that only high spatial frequencies with $\tilde{f} > 10/(2\pi r_0)$ are involved in the loss increase. In conclusion, Figure 6 provides a visual interpretation of the impact of transverse roughness on confinement loss. It establishes that only roughness components with high spatial frequencies, corresponding to DM azimuthal index $\mu > 10$ contribute to additional confinement loss, as they satisfy the phase-matching condition for coupling with leaky dielectric modes. The colored regions in the figure illustrate the spectral correspondence between roughness periodicity and transmission bands, highlighting why low-frequency roughness does not significantly affect CL. This has important implications in case of non-sinusoidal perturbations. As will be shown in the next section, it is not the whole spectrum of the t-roughness that is involved, but only its high-frequency range.

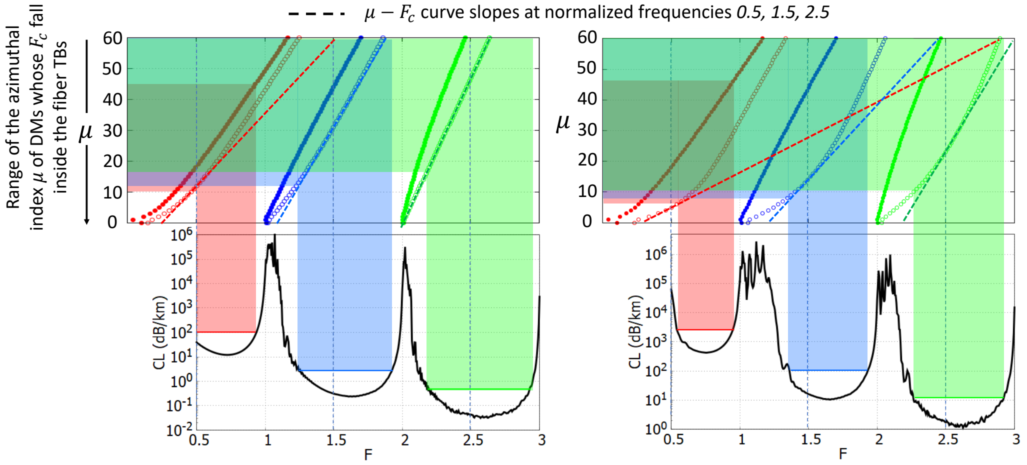

Figure 6. Spatial period ranges involved in the TBs of Fibers #1 (**left**) and #2 (**right**). Red, blue and green colored regions show how the TBs (**bottom**) are linked to the spatial periods through the $\mu - F_c$ curves (**top**). In particular, only perturbations with a number of periods $P = \mu$ greater than 10 give a TB loss contribution. Dashed kines show the $\mu - F_c$ curve slopes at the normalized frequencies $F = 0.5, 1.5, 2.5$.

For the sake of completeness, it must be remarked that, in principle, the spatial periods giving a contribution also have an upper bound, as it can be seen, e.g., in Figure 6. As an example, for Fiber #2 in the TB between $F = 1$ and $F = 2$, the upper bound corresponds to $P = 50$. However, by taking into account that real PSDs decay for increasing spatial frequency, the upper bounds correspond to spatial frequencies so high that the corresponding roughness spectrum values are very low, enough that they can be neglected in the analysis.

4. Random Corrugation

To take into account the stochastic nature of real roughness, the same treatment proposed in [33] is employed here, but with an adaptation to periodic roughness. Let Δr be a random variable described by a PSD $S(\tilde{f})$ where $\tilde{f}$ is the spatial frequency. For geometrical reasons, Δr is periodic with a period $2\pi r_0$ and the PSD is thus defined over a discrete set of frequencies $\tilde{f}_P = m\tilde{f}_0$ which are multiples of the fundamental one $\tilde{f}_0 = 1/(2\pi r_0)$. Δr can be written as follows:

$$\Delta r(\theta) = A \sum_{m=1}^{\infty} \sqrt{S(m\tilde{f}_0)} \cos(m\theta + \phi_P) \tag{21}$$

where ϕ_m is a random variable uniformly distributed between 0 and 2π. By exploiting Euler's formula: $\cos(m\theta + \phi_m) = 1/2e^{j\phi_m}e^{jm\theta} + 1/2e^{-j\phi_m}e^{-jm\theta}$, the C_m coefficients in Equation (8) can be written with the following expression:

$$C_m = \frac{A}{2}\sqrt{S(m\tilde{f}_0)}\; e^{-j\phi_m m/|m|}. \tag{22}$$

The loss calculation for TLFs affected by random t-roughness is obtained by applying a independent random corrugation on each tube interface, by performing ten independent simulations, and by calculating the average value for each frequency.

First of all, let us consider a "*white*" random roughness; that is, one described by a constant PSD:

$$S(\tilde{f}) = S_0 \quad \forall \tilde{f}. \tag{23}$$

An example is shown in Figure 7a where $S_0 = 6 \times 10^{-3}$ nm^2. Even though it corresponds to a non-physical process, as the corresponding root mean square (RMS) value is infinite, this process is useful to separate the frequency dependence of the FCM-DM coupling from the PSD one.

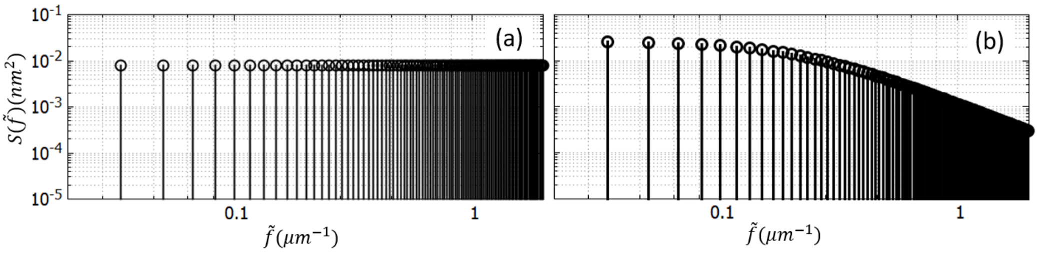

Figure 7. PSD versus spatial frequency. (**a**) "White" roughness. (**b**) Roughness having an exponential autocorrelation function.

Figure 8a compares the loss of the ideal Fiber #1 and the same with t-roughness with different values of S_0. In both the fibers, with the exception of the fundamental TB, for a given S_0 the TB minima have almost the same values irrespective of the TB order. This is coherent with the discussion of the scaling laws from Section 2.3 and Equation (16). The minima values are also independent of the kind of the fiber (TLF or nested). In fact, according to Equation (11), the additional loss $\delta\alpha$ does not depend on the FCM loss of the ideal fiber. In conclusion, Figure 8 further confirms that only the high-frequency spectral components of roughness contribute to loss, while lower-frequency components have minimal impact. The observed trend in the curves, where loss consistently increases with the amplitude of the roughness PSD, validates the model's key prediction: confinement loss enhancement is determined by the spectral distribution of transverse roughness rather than its total amplitude (RMS value). Moreover, the additional confinement loss induced by roughness is independent of the intrinsic confinement strength of the cladding design, as demonstrated by the similar roughness-induced loss increase observed in both the tube lattice fiber (TLF) and the nested fiber. Finally, as expected by the model, α_{tr} is directly proportional to S_0 (see Equations (8), (12), and (22)). For the considered fiber, the relationship is

$$\delta\alpha(\mathrm{dB/km}) = 500 S_0(\mathrm{nm}^2). \tag{24}$$

The effects of t-roughness are negligible if $\alpha_{tr} < \alpha_{FCM_0}$. Propagation losses lower than 0.1 dB/km are just a step ahead in the near-infrared region [3]. With those values, t-roughness effects are negligible if the PSD value is lower than 2×10^{-4} nm^2.

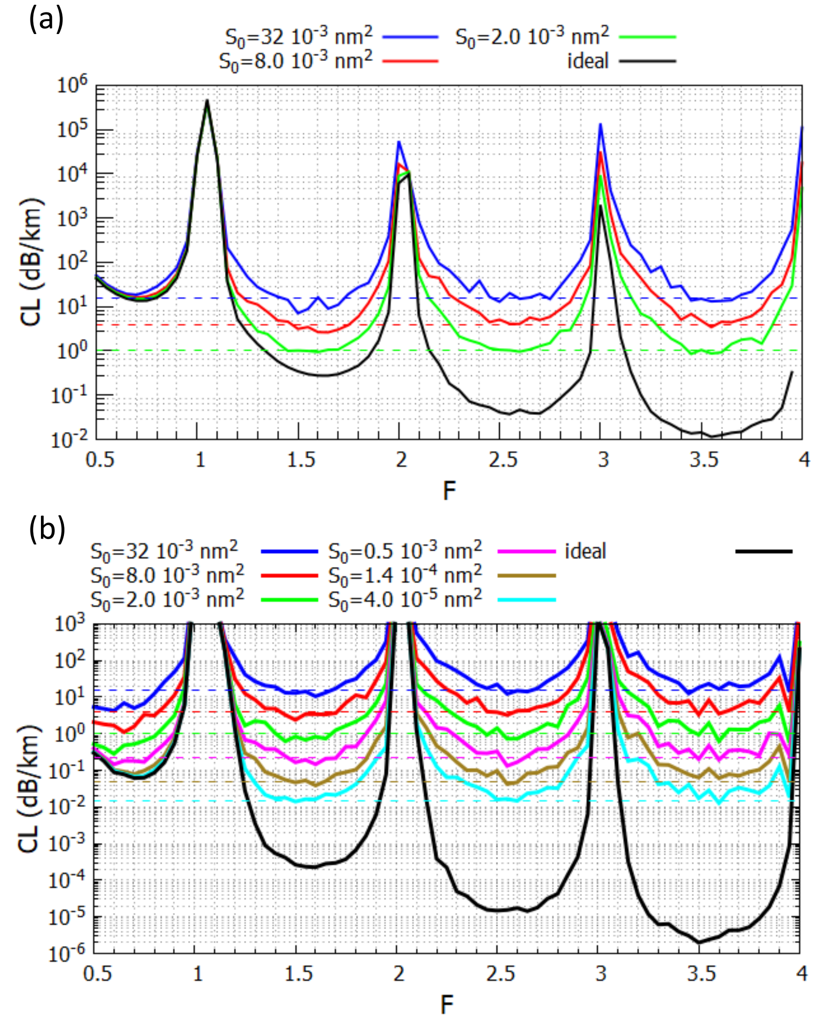

Figure 8. Fibers affected by t-roughness with "white" PSD. Losses of (**a**) Fiber #1 and of (**b**) the corresponding nested TLF having $r_{nested} = 0.5 r_{ext}$ are reported for different S_0 values and for the ideal TLFs. Dashed lines highlight the loss minima values for each S_0 value, obtained from Equation (24).

The fundamental TB (FTB) is a different matter. In the TLF, α_{FCM_0} is higher than any α_{tr} corresponding to the S_0 here considered; thus, the t-roughness effects are not observable. The effects are visible in the nested fiber and the minima values are lower than those of the other TBs. This is in contrast with the scaling laws discussed in Section 2.3 and the trends in the other TBs. To understand this apparent anomaly, it is necessary to recall that the final value of α_{tr} is also given by the contribution of the lateral tails of the function $L(F)$. When DM contributions $\delta\alpha_i$ are spectrally dense (the F_{c_i} are very close each other), each peak is overlapping with the tails of a number of adjacent peaks. If the spectral density is reduced, the same happens for the tail overlap and α_{tr}. Observing the $\mu - F_c$ curves in the first TB (corresponding to radial index $\nu = 0$), the slopes are lower than those of higher-order TBs [30], resulting in a lower spectral density of DMs and a lower α_{tr}.

White PSD cannot describe a real roughness. There are different proposals about the roughness PSD in hollow-core fibers. Here, we consider a stochastic process with an exponential auto-correlation function having correlation length L_c. The corresponding PSD is

$$S(m\tilde{f}_0) = \sigma^2 \frac{r_0}{m_c} \frac{1}{1 + \left(\frac{m}{2\pi m_c}\right)^2}, \tag{25}$$

where σ is the RMS value, and m_c is the cutoff parameter such that $\tilde{f}_{m_c} = \tilde{f}_c = 1/(2\pi L_c)$. An example with parameters $\sigma = 1$ nm, $m_c = 40$ and $r_0 = 12$ µm is shown in Figure 7b. For low spatial frequencies ($\tilde{f} < \tilde{f}_c$), the PSD is approximately constant, whereas for $\tilde{f} > \tilde{f}_c$ it tends to decay with a rate of $1/\tilde{f}^2$. As highlighted in the previous section, not all the spatial frequencies contribute to the additional loss in the TBs. To validate this result also in the case of random roughness, Fiber #1 was investigated by considering different PSDs having different σ, and different cutoff m_c, but the same values at high frequencies. The results are shown in Figure 9. The light-blue area shows the spectral range where $m \geq 10$. Three PSDs have almost the same values in this range, whereas the fourth has a lower value up to $m \sim 25$.

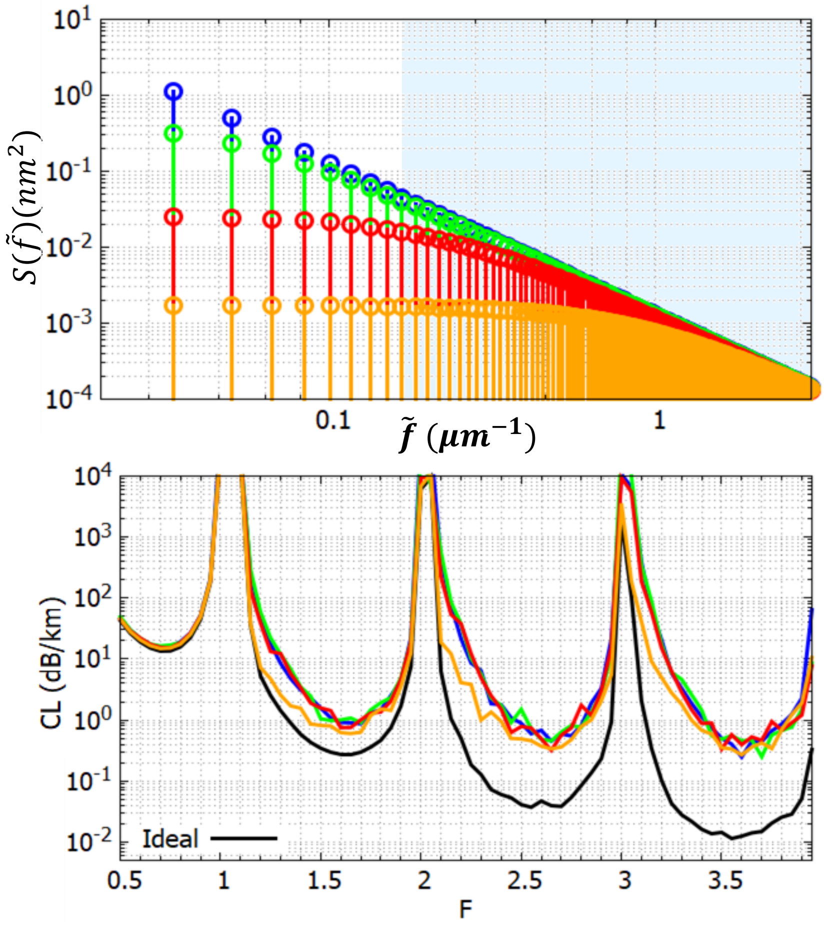

Figure 9. Fiber #1 affected by t-roughness with different RMS σ and cutoff m_c, but the same PSD for $P > 10$ except for the orange one. PSD parameters are: $\sigma = 2.7$ nm and $m_c = 1$ (blue); $\sigma = 1.4$ nm and $m_c = 20$ (green); $\sigma = 0.7$ nm and $m_c = 80$ (red); $\sigma = 0.35$ nm and $m_c = 330$ (orange). **Top**: PSD functions. **Bottom**: Losses of the ideal TLF and of the one affected by t-roughness. Same colors refer to same PSD parameters.

The losses caused by the fist three PSD functions are almost perfectly overlapping. The fourth shows lower values up to the center of the TBs and reaches the same values as the others in the second half of the TBs, corresponding to the cutoffs of DMs having $\mu \geq 25$.

The results agree perfectly with the model and confirm that the losses caused by t-roughness are not directly related to either the RMS value or the cutoff, but only to the PSD values at high spatial frequencies. PSD values at low frequencies do not play any role in defining the loss caused by t-roughness. Figure 10 compares the effects of PSDs having the same RMS $\sigma = 1.0$ nm and different cutoffs $m_c = 1, 10, 40$. As expected, the loss enhancement is not proportional to m_c, because the PSD values at high frequencies are not. In particular, notice that by comparing the PSDs having $m_c = 1$ and $m_c = 40$, the former has much higher values at low frequencies than the latter, but the corresponding losses are lower, since the values at high frequencies are.

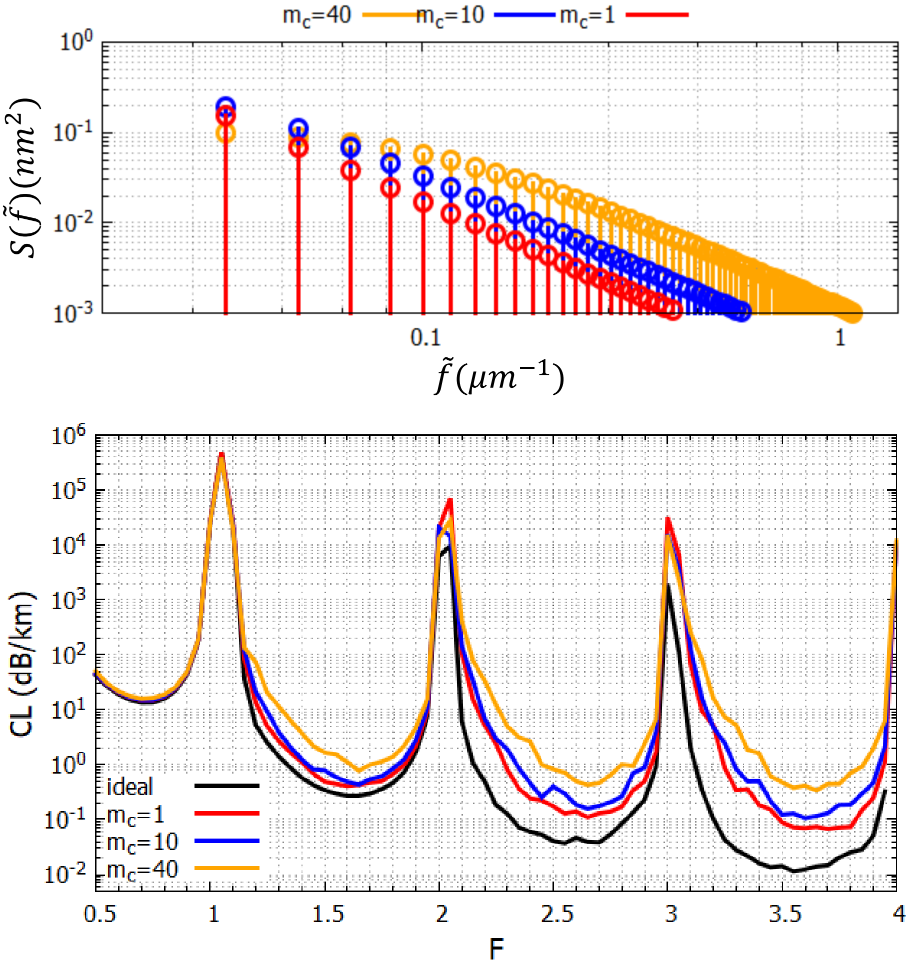

Figure 10. Fiber #1 affected by t-roughness having $\sigma = 1.0$ nm and three different cutoffs: $m_c = 1,\ 10,\ 40$. **Top**: PSD functions. **Bottom**: loss of the ideal TLF and of the TLFs affected by the corresponding t-roughness.

5. Conclusions

In this work, a model for the analysis and investigation of the effects of tube surface roughness along the transverse direction in HC-TLFs was proposed and validated. The model is based on coupled mode theory and azimuthal Fourier decomposition, and it shows that roughness causes additional loss through the coupling between FCM and DMs. It has been validated by considering both a deterministic sinusoidal corrugation and a stochastic roughness with exponential autocorrelation function. The theory is in agreement with the numerical results, showing that the additional loss depends on the spectral content of the t-roughness PSD at high frequencies irrespective of the RMS value, that it scales as the inverse of the cube of the core radius and that it is independent of the wavelength. Fibers with low loss in the ideal case, such as nested ones, are especially sensitive to t-roughness. To guarantee that t-roughness effects are negligible even for losses lower than 0.1 dB/km, the PSD at spatial frequencies higher than $10/(2\pi r_0)$ should be lower than 0.2 nm^2. These findings provide a clear guideline for optimizing the optical fiber fabrication process. Since the high-frequency roughness components contribute to confinement loss, they might be a limiting factor for ultra-low confinement loss fiber. Consequently, manufacturing techniques should focus on minimizing fine-scale surface irregularities to mitigate surface roughness-induced confinement loss. Recent techniques to control surface roughness [1] could be useful. Additionally, roughness characterization [20] should not be only limited to assess the total roughness amplitude but also analyze its spectral content to ensure that high-frequency components remain below the critical threshold identified in this study. By incorporating these considerations, fiber fabrication processes can be optimized to maintain ultra-low-loss performance in inhibited coupling fibers.

Author Contributions: Conceptualization, L.V. and F.B.; methodology, L.V. and F.M.; software, L.R. and K.V.; validation, F.M., L.V. and F.B.; formal analysis, L.V. and F.M.; investigation, F.M., L.R. and K.V.; data curation, F.M. and K.V.; writing—original draft preparation, F.M., L.V. and L.R.; writing—review and editing, F.M., L.V., L.R., K.V. and F.B.; visualization, F.M.; supervision, L.V.; project administration, L.V. All authors have read and agreed to the published version of the manuscript.

Funding: This work was supported by the European Commission through the H2020-FETOPEN-2018-2020 project CRYST3, Grant No. 964531.

Data Availability Statement: The original data presented in the study are openly available in Zenodo at https://doi.org/10.5281/zenodo.13971489

Conflicts of Interest: The authors declare no conflict of interest.

References

1. Osório, J.H.; Amrani, F.; Delahaye, F.; Dhaybi, A.; Vasko, K.; Melli, F.; Giovanardi, F.; Vandembroucq, D.; Tessier, G.; Vincetti, L.; et al. Hollow-core fibers with reduced surface roughness and ultralow loss in the short-wavelength range. *Nat. Comm.* **2023**, *14*, 1146. [CrossRef]
2. Jasion, G.; Sakr, H.; Hayes, J.; Sandoghchi, S.; Hooper, L.; Numkam Fokoua, E.; Saljoghei, A.; Mulvad, H.; Alonso, M.; Taranta, A.; et al. 0.174 dB/km Hollow Core Double Nested Antiresonant Nodeless Fiber (DNANF). In Proceedings of the 2022 Optical Fiber Communications Conference and Exhibition (OFC), San Diego, CA, USA, 6–10 March 2022; pp. 1–3.
3. Chen, Y.; Petrovich, M.; Fokoua, E.N.; Adamu, A.I.; Hassan, M.R.B.A.; Sakr, H.; Gorajoobi, S.B.; Alonso, M.; Ando, R.F.; Papadimopoulos, A.; et al. Hollow Core DNANF Optical Fiber with < 0.11 dB/km Loss. In Proceedings of the 2024 Optical Fiber Communications Conference and Exhibition (OFC), San Diego, CA, USA, 24–28 March 2024; pp. 1–3.
4. Gao, S.; Chen, H.; Sun, Y.; Xiong, Y.; Yang, Z.; Zhao, R.; Ding, W.; Wang, Y. Fourfold truncated double-nested antiresonant hollow-core fiber with ultralow loss and ultrahigh mode purity. *Optica* **2025**, *12*, 56–61. [CrossRef]
5. Wang, Y.Y.; Wheeler, N.V.; Couny, F.; Roberts, P.J.; Benabid, F. Low loss broadband transmission in hypocycloid-core Kagome hollow-core photonic crystal fiber. *Opt. Lett.* **2011**, *36*, 669–671. [CrossRef] [PubMed]
6. Vincetti, L.; Setti, V.; Zoboli, M. Terahertz Tube Lattice Fibers With Octagonal Symmetry. *IEEE Photonics Technol. Lett.* **2010**, *22*, 972–974. [CrossRef]
7. Pryamikov, A.D.; Biriukov, A.S.; Kosolapov, A.F.; Plotnichenko, V.G.; Semjonov, S.L.; Dianov, E.M. Demonstration of a waveguide regime for a silica hollow-core microstructured optical fiber with a negative curvature of the core boundary in the spectral region > 3.5 µm. *Opt. Express* **2011**, *19*, 1441–1448. [CrossRef]
8. Belardi, W.; Knight, J.C. Negative curvature fibers with reduced leakage loss. In Proceedings of the OFC 2014, San Diego, CA, USA, 9–13 March 2014; pp. 1–3. [CrossRef]
9. Poletti, F. Nested antiresonant nodeless hollow core fiber. *Opt. Express* **2014**, *22*, 23807–23828. [CrossRef] [PubMed]

10. Gao, S.f.; Wang, Y.y.; Ding, W.; Jiang, D.l.; Gu, S.; Zhang, X.; Wang, P. Hollow-core conjoined-tube negative-curvature fibre with ultralow loss. *Nat. Commun.* **2018**, *9*, 2828. [CrossRef]
11. Cregan, R.F.; Mangan, B.J.; Knight, J.C.; Birks, T.A.; Russell, P.S.J.; Roberts, P.J.; Allan, D.C. Single-Mode Photonic Band Gap Guidance of Light in Air. *Science* **1999**, *285*, 1537–1539. [CrossRef]
12. Poletti, F.; Petrovich, M.N.; Richardson, D.J. Hollow-core photonic bandgap fibers: Technology and applications. *Nanophotonics* **2013**, *2*, 315–340. [CrossRef]
13. Wheeler, N.V.; Petrovich, M.N.; Slavík, R.; Baddela, N.; Numkam, E.; Hayes, J.R.; Gray, D.R.; Poletti, F.; Richardson, D.J. Wide-bandwidth, low-loss, 19-cell hollow core photonic band gap fiber and its potential for low latency data transmission. In Proceedings of the National Fiber Optic Engineers Conference. Optica Publishing Group, Los Angeles, CA, USA, 4–8 March 2012; p. PDP5A.2. [CrossRef]
14. Melli, F.; Rosa, L.; Vincetti, L. Analytical Formulas for Micro-Bending and Surface Scattering Loss Estimation in Tube Lattice Fibers. *J. Light. Technol.* **2023**, *41*, 5714–5721. [CrossRef]
15. Fokoua, E.N.; Mousavi, S.A.; Jasion, G.T.; Richardson, D.J.; Poletti, F. Loss in hollow-core optical fibers: Mechanisms, scaling rules, and limits. *Adv. Opt. Photon.* **2023**, *15*, 1–85. [CrossRef]
16. Roberts, P.J.; Couny, F.; Sabert, H.; Mangan, B.J.; Williams, D.P.; Farr, L.; Mason, M.W.; Tomlinson, A.; Birks, T.A.; Knight, J.C.; et al. Ultimate low loss of hollow-core photonic crystal fibres. *Opt. Express* **2005**, *13*, 236–244. [CrossRef] [PubMed]
17. Bresson, B.; Brun, C.; Buet, X.; Chen, Y.; Ciccotti, M.; Gâteau, J.; Jasion, G.; Petrovich, M.N.; Poletti, F.; Richardson, D.J.; et al. Anisotropic Superattenuation of Capillary Waves on Driven Glass Interfaces. *Phys. Rev. Lett.* **2017**, *119*, 235501. [CrossRef] [PubMed]
18. Roberts, P.J.; Couny, F.; Sabert, H.; Mangan, B.J.; Birks, T.A.; Knight, J.C.; Russell, P.S.J. Loss in solid-core photonic crystal fibers due to interface roughness scattering. *Opt. Express* **2005**, *13*, 7779–7793. [CrossRef]
19. Fokoua, E.N.; Poletti, F.; Richardson, D.J. Analysis of light scattering from surface roughness in hollow-core photonic bandgap fibers. *Opt. Express* **2012**, *20*, 20980–20991. [CrossRef]
20. Dhaybi, A.; Osório, J.; Vasko, K.; Amrani, F.; Tessier, G.; Debord, B.; Gérôme, F.; Benabid, F. Picometer-resolution and high dynamic-range profilometer for hollow-core fiber surface roughness characterization. In Proceedings of the European Conference on Lasers and Electro-Optics, Optica Publishing Group, Munich, Germany, 26–30 June 2023; p. cj_4_2.
21. Buet, X.; Brun, C.; Gâteau, J.; Bresson, B.; Sandoghchi, S.R.; Fokoua, E.N.; Petrovich, M.; Poletti, F.; Richardson, D.; Vandembroucq, D.; et al. Nondestructive measurement of the roughness of the inner surface of hollow core-photonic bandgap fibers. *Opt. Lett.* **2016**, *41*, 5086–5089. [CrossRef]
22. Brun, C.; Buet, X.; Bresson, B.; Capelle, M.S.; Ciccotti, M.; Ghomari, A.; Lecomte, P.; Roger, J.P.; Petrovich, M.N.; Poletti, F.; et al. Picometer-scale surface roughness measurements inside hollow glass fibres. *Opt. Express* **2014**, *22*, 29554–29567. [CrossRef]
23. Phan-Huy, M.C.; Moison, J.M.; Levenson, J.A.; Richard, S.; Melin, G.; Douay, M.; Quiquempois, Y. Surface Roughness and Light Scattering in a Small Effective Area Microstructured Fiber. *J. Light. Technol.* **2009**, *27*, 1597–1604. [CrossRef]
24. Melli, F.; Vasko, K.; Rosa, L.; Benabid, F.; Vincetti, L. Transverse Roughness: Modeling and Effects Analysis on Inhibited Coupling Fibers. In Proceedings of the Advanced Photonics Congress 2024, Optica Publishing Group, Québec City, QC, Canada, 28 July–1 August 2024; p. SoM3F.6. [CrossRef]
25. Melli, F.; Vasko, K.; Rosa, L.; Benabid, F.; Vincetti, L. Analytical framework for mode-coupling in hollow-core inhibited-coupling fibers. *J. Lighwave Technol.* **2025.** [CrossRef]
26. Vincetti, L.; Rosa, L. A simple analytical model for confinement loss estimation in hollow-core Tube Lattice Fibers. *Opt. Express* **2019**, *27*, 5230–5237. [CrossRef]
27. Haus, H.; Huang, W.; Kawakami, S.; Whitaker, N. Coupled-mode theory of optical waveguides. *J. Light. Technol.* **1987**, *5*, 16–23. [CrossRef]
28. Okamoto, K. Chapter 4—Coupled mode theory. In *Fundamentals of Optical Waveguides*, 2nd ed.; Okamoto, K., Ed.; Academic Press: Burlington, UK, 2006; pp. 159–207. [CrossRef]
29. Melli, F.; Vasko, K.; Rosa, L.; Benabid, F.; Vincetti, L. Azimuthal Fourier decomposition for loss analysis of hollow-core tube lattice fibers part I: Ideal fibers. *Results Opt.* **2024**, *15*, 100657. [CrossRef]
30. Kharadly, M.; Lewis, J. Properties of dielectric-tube waveguides. *Proc. Inst. Electr. Eng.* **1969**, *116*, 214–224.
31. Vincetti, L. Empirical formulas for calculating loss in hollow core tube lattice fibers. *Opt. Express* **2016**, *24*, 10313–10325. [CrossRef]
32. Melli, F.; Giovanardi, F.; Vasko, K.; Rosa, L.; Benabid, F.; Vincetti, L. Azimuthal Fourier decomposition for loss analysis of hollow-core tube lattice fibers, Part II: Tube thickness variation effects. *Results Opt.* **2024**, *16*, 100726. [CrossRef]
33. Jin, X.; Payne, F.P. Numerical Investigation of Microbending Loss in Optical Fibres. *J. Light. Technol.* **2016**, *34*, 1247–1253. [CrossRef]